Superscattering from Subwavelength Corrugated Cylinders

Vitalii I. Shcherbinin,[1,2] Volodymyr I. Fesenko,[1,3] Tetiana I. Tkachova,[2] and Vladimir R. Tuz[1,3,*]

[1] *State Key Laboratory of Integrated Optoelectronics, College of Electronic Science and Engineering, International Center of Future Science, Jilin University, 2699 Qianjin Street, Changchun, 130012, China*

[2] *National Science Center "Kharkiv Institute of Physics and Technology", National Academy of Sciences of Ukraine, 1 Akademicheskaya Street, Kharkiv, 61108, Ukraine*

[3] *Institute of Radio Astronomy, National Academy of Sciences of Ukraine, 4 Mystetstv Street, Kharkiv, 61002, Ukraine*

(Received 5 December 2019; accepted 7 February 2020; published 28 February 2020)

Wave scattering from a cylinder with a tensor impedance surface is investigated on the basis of the Lorentz-Mie theory. A practical example of such a cylinder is a subwavelength metallic rod with helical dielectric-filled corrugations. The investigation is performed with the aim to maximize the scattering cross section by tailoring the surface impedance of cylindrical scatterers. For normally incident TE_z and TM_z waves, the required surface impedance of a subwavelength cylinder can be produced by longitudinal (axial) and transverse (circumferential) corrugations, respectively. It is shown that such corrugations induce superscattering at multiple frequencies, which can be widely tuned with either the size or the permittivity of dielectric-filled corrugations or both. In the microwave band, this effect is demonstrated to be robust to material losses and is validated against full-wave simulations and experimental results. For TE_z waves the enhanced scattering from the cylinder is found to have a broad frequency bandwidth, provided that the relative permittivity of corrugations is low or equal to unity. In the latter case, the corrugated cylinder acts as an all-metal superscatterer. For such cylinders, near-field measurements are performed and provide experimental evidence of the superscattering phenomenon for all-metal objects. In addition to multifrequency superscattering, the dielectric-filled corrugations are shown to provide multifrequency cloaking of the cylinder for incident TM_z waves. Simultaneous superscattering and cloaking at multiple frequencies distinguishe corrugated cylinders from other known practicable scatterers for potential applications in antenna designing, sensing, and energy harvesting.

DOI: 10.1103/PhysRevApplied.13.024081

Enhancement of wave scattering from small objects is a vital issue in present-day technologies [1–7], including miniaturized antennas, sensors, and energy-harvesting devices. This issue is directly related to the natural constraint inherent in most subwavelength scatterers [8]. This constraint is known as a single-channel limit [9], which is an upper limit to the scattering cross section for such scatterers and is attained under the resonance condition for one of the scattering modes (channels). The only way to overcome this constraint is to ensure resonant scattering of several modes at a single frequency. Such a resonance overlap magnifies scattering from a given object and is known as "superscattering" [9,10]. The greater the number of resonant modes, the larger the superscattering cross section. Therefore, theoretically, superscattering opens a way to arbitrarily enhanced wave scattering from subwavelength objects. In practice, however, this effect is often hindered by the lack of low-loss materials and appropriate design solutions.

In the infrared and visible parts of spectrum, superscattering can be realized in cylindrical structures formed by several plasmonic and dielectric layers. In pioneering work [9], for such a structure the total scattering cross section was optimized to exceed the single-channel limit by a factor of 8. However, in actual conditions, the enhancement of wave scattering from this scatterer appears to be 4 times lower [9] or even disappears [11]. The reason is losses in plasmonic material (metal). A similar effect was reported in Ref. [11] for a core-shell plasmonic nanowire, which exhibits a scattering cross section slightly in excess of the single-channel limit in the presence of material losses. The situation is much the same for terahertz frequencies. In this frequency band, the plasmonic component of superscatterers can be replaced by conducting materials such as graphene [12,13] or hexagonal boron nitride (BN) [14], which can initiate resonance overlap for different scattering modes. However, losses in these materials notably degrade

*tvr@jlu.edu.cn

the performance of such scatterers, making efficient superscattering practically elusive in the terahertz band. The effect of losses is of minor importance for good conductors (metals) in the microwave band. Their use as microwave superscatterers, however, is hampered by the fact that metals on their own do not support any scattering resonances due to small surface impedance. The required low-loss surface impedance can be realized in all-metal or metal-dielectric metasurfaces [15]. Such metasurfaces are usually made in the form of periodic arrays of subwavelength elements (strips, crosses, patches, etc. [16]), which can be fabricated by patterning a metallic layer. The advantageous use of metasurfaces composed of circumferential metallic strips was recently demonstrated by the first experimental evidence of superscattering in Ref. [17], in which the measured scattering cross section was reported to be about 5 times the single-channel limit. This impressive result offers great prospects for practical use of superscatterers in the microwave band.

The experimental findings in Ref. [17] are related to scattering from a multilayered metasurface-dielectric cylinder, when the electric field vector of an incident wave is oriented along the cylinder symmetry axis (TM_z waves in our notations). Multilayered structures made of alternating plasmonic-dielectric [9–11,18], graphene-dielectric [12,13], BN-dielectric [14], dielectric-dielectric [19] or metasurface-dielectric [17] layers are the most common design solution for cylindrical superscatterers. This raises the following questions: Is it possible to realize a superscatterer of simpler design with a single surface (metasurface)? Is it possible to achieve superscattering without a dielectric? Is it possible to design an efficient superscatterer for TE_z waves in the microwave band? Our answer is yes in all cases. All this is possible with a subwavelength corrugated cylinder. It has long been known that such a cylinder is characterized by an averaged surface impedance [20–25], which may induce scattering resonances associated with the so-called spoof (or designer) surface plasmons [26]. In this paper, we show that properly designed corrugations ensure overlapping of these resonances, resulting in superscattering.

I. SCATTERING FROM A TENSOR IMPEDANCE CYLINDER

Consider an arbitrarily polarized plane wave propagated in space with relative permittivity ε_2 and permeability $\mu_2 = 1$. The wave has frequency ω and is normally incident on a cylinder of radius R. In cylindrical coordinates $\{r, \varphi, z\}$, the total field of incident and scattered waves can be expanded in terms of azimuth modes as [27]

$$\begin{Bmatrix} H_{z2} \\ E_{z2} \end{Bmatrix} = \sum_{n=-\infty}^{\infty} i^n H_0 F_n \left(\begin{Bmatrix} 1 \\ P \end{Bmatrix} J_n(k_2 r) + \begin{Bmatrix} a_n \\ b_n \end{Bmatrix} H_n^{(1)}(k_2 r) \right), \tag{1}$$

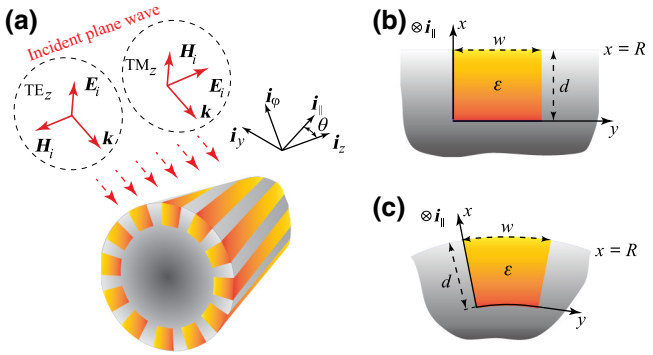

FIG. 1. (a) Metallic cylinder with helical dielectric-filled corrugations, and structure of (b) rectangular and (c) wedge-shaped corrugations.

where $F_n = \exp(-i\omega t + in\varphi)$, $J_n(\cdot)$ is the Bessel function, $H_n^{(1)}(\cdot)$ is the Hankel function of the first kind, n is the azimuth index, which numerates scattering modes (channels), $k_2 = \sqrt{\varepsilon_2}k$, where $k = \omega/c$, $\{a_n, b_n\}$ are the dimensionless amplitudes of the scattered wave, and $H_{zi} = H_0 = [0.5(1+Q)]^{1/2}$ and $E_{zi} = PH_0 = [0.5(1-Q)]^{1/2}\exp(i\beta)$ are the amplitudes of the incident wave, where $Q \in [-1, 1]$, $\beta \in [-\pi, \pi]$, where Q defines the polarization of incident wave and is 1, -1, and 0 for TE_z, TM_z, and dual-polarized waves [see Fig. 1(a)], respectively.

The unknowns a_n and b_n are determined by the boundary conditions on the cylinder surface. For generality, assume that the cylindrical scatterer features a tensor surface impedance such that

$$\begin{aligned} E_{\varphi 2} &= Z_{\varphi\varphi} H_{z2} - Z_{\varphi z} H_{\varphi 2}, \\ E_{z2} &= -Z_{zz} H_{\varphi 2} + Z_{z\varphi} H_{z2} \end{aligned} \tag{2}$$

for $r = R$.

In this case, substitution of Eq. (1) into Eq. (2) gives the following explicit expressions for the scattering coefficients:

$$\begin{aligned} a_n = &-\left[\left(\lambda_1 + Z_{\varphi\varphi} - \varepsilon_2 P Z_{\varphi z}\lambda_1\right)\left(1 + \varepsilon_2 Z_{zz}\lambda_2\right)\right. \\ &\left. - \varepsilon_2 Z_{\varphi z}\lambda_2\left(P + \varepsilon_2 P Z_{zz}\lambda_1 - Z_{z\varphi}\right)\right]\lambda_3 D^{-1}, \\ b_n = &-\left[\left(\lambda_2 + Z_{\varphi\varphi}\right)\left(P + \varepsilon_2 P Z_{zz}\lambda_1 - Z_{z\varphi}\right)\right. \\ &\left. + Z_{z\varphi}\left(\lambda_1 + Z_{\varphi\varphi} - \varepsilon_2 P Z_{\varphi z}\lambda_1\right)\right]\lambda_3 D^{-1}, \end{aligned} \tag{3}$$

where $D = \left(\lambda_2 + Z_{\varphi\varphi}\right)\left(1 + \varepsilon_2 Z_{zz}\lambda_2\right) - \varepsilon_2 Z_{\varphi z} Z_{z\varphi}\lambda_2$, $\lambda_1 = ikk_2^{-1} J_n'(k_2 R)/J_n(k_2 R)$, $\lambda_2 = ikk_2^{-1} H_n'^{(1)}(k_2 R)/H_n^{(1)}(k_2 R)$, and $\lambda_3 = J_n(k_2 R)/H_n^{(1)}(k_2 R)$.

With the amplitudes a_n and b_n, one obtains the scattering efficiency [27]

$$Q_{\text{sca}} = \frac{2}{kR} N_{\text{sca}} = \frac{2}{kR\left(1 + |P|^2\right)} \sum_{n=-\infty}^{\infty} \left(|a_n|^2 + |b_n|^2\right), \tag{4}$$

where $N_{\rm sca}$ is the scattering cross section normalized to the single-channel scattering limit $2\lambda/\pi$ [8,9]. Both $Q_{\rm sca}$ and $N_{\rm sca}$ serve as a measure of wave scattering from an impedance cylinder of radius R.

For clarity, it is convenient to rewrite the expressions in Eq. (3) in the following form [8,28]:

$$a_n = \frac{U_n^{\rm TE}}{U_n^{\rm TE} + iV_n^{\rm TE}}, \quad b_n = \frac{U_n^{\rm TM}}{U_n^{\rm TM} + iV_n^{\rm TM}}, \tag{5}$$

where U_n and V_n are the real-valued functions in the lossless case.

In this case, the scattering coefficients are bounded quantities, which attain the peak values $|a_n| = 1$ and $|b_n| = |P|$ at resonance $V_n = 0$ [8]. Under the resonance condition, the scattering cross section of the nth azimuth mode reaches the single-channel limit [9], which corresponds to the highest possible level of wave scattering for most subwavelength objects. A way to overcome this limit for small scatterers is to ensure resonance overlap for two or more scattering channels. This phenomenon is known as "superscattering" [9,10]. In a similar manner, it is possible to achieve cloaking of a subwavelength object, provided that the conditions $U_n = 0$ are satisfied for dominant (low-order) scattering modes [15,28–32]. Despite the limitation on the scattering cross section, smaller resonant objects can scatter waves more efficiently than nonresonant scatterers of the same dimensions [see Eq. (4)]. A widely known example of a highly efficient scatterer is an atom at resonant frequency [9].

Theoretically, a tensor impedance surface furnishes the most-general way to manipulate scattering from the object with incident arbitrarily polarized waves. However, in modern practice, there are only a few ways to design and tailor such a surface (metasurface). One way is to introduce a patterned metallic coating on a dielectric substrate [33–35]. In the cylindrical geometry, an example is a dielectric wire coated by helical conducting strips [32,36]. An alternative design solution is described in the Appendix. It is in the form of a subwavelength metallic rod with helical periodic corrugations [Fig. 1(a)].

One of the means of manipulating wave scattering from a cylinder involves off-diagonal components $Z_{\varphi z}$ and $Z_{z\varphi}$ of the surface impedance tensor. This is because these components give rise to a cross-polarization coupling [see Eq. (3)] and thereby enable polarization conversion of waves normally incident on the cylinder. In other words, tensor impedance metasurfaces make it possible to manipulate the polarization of scattered waves [33,37] and thereby may increase the functionality of the scatterer. Although the problem of polarization control by metasurfaces is of much current interest [38–41], it deserves detailed consideration, but this is beyond the scope of the present investigation. In the following, we aim to enhance scattering of TE_z and TM_z waves from a cylinder by means of surface impedance, which induces no cross-polarization coupling. To attain this goal, we take advantage of longitudinal wedge-shaped and transverse ring-shaped corrugations (see the Appendix for more details). The corrugations considered have period p, width w, depth d, and are filled with a dielectric of permittivity ε.

II. SUPERSCATTERING OF TE_z WAVES

First, we consider a TE_z wave ($Q = 1$) normally incident on a perfectly-electrically-conducting (PEC) cylinder with longitudinal ($\mathbf{i}_\parallel \parallel \mathbf{i}_z$) wedge-shaped corrugations [Fig. 1(c)] described by an averaged anisotropic surface impedance with a single nonzero component:

$$Z_{\varphi\varphi} = -\frac{w}{p}\frac{ik}{k_\perp}\frac{J_0'(k_\perp R) - BN_0'(k_\perp R)}{J_0(k_\perp R) - BN_0(k_\perp R)}, \tag{6}$$

where $k_\perp = \sqrt{\varepsilon}k$ and $B = J_0'(k_\perp R_d)/N_0'(k_\perp R_d)$, where $R_d = R - d$, and $N_m(\cdot)$ denotes the mth order Neumann function [for the derivation of Eq. (6) see the Appendix]. The aim is to investigate the ability of such corrugations to enhance wave scattering from the cylinder in free space ($\varepsilon_2 = 1$, $\mu_2 = 1$).

Figures 2(a) and 2(b) show the scattering efficiency $Q_{\rm sca}$ and normalized scattering cross section $N_{\rm sca}$ as functions of the radius R and surface impedance $Z_{\varphi\varphi}$ of the subwavelength cylinder. It can be seen that the smaller the scatterer radius, the greater the value of $\mathrm{Im}\, Z_{\varphi\varphi}$ required to attain the maximum $Q_{\rm sca}$. Besides, smaller corrugated cylinders scatter waves more efficiently than smooth PEC rods ($Z_{\varphi\varphi} = 0$) of the same radius and, in this regard, can be considered as so-called electromagnetic meta-atoms [9]. However, the total scattering cross section of such meta-atoms falls below the single-channel limit ($N_{\rm sca} = 1$) for very small R [Fig. 2(b)]. Thus, the radius of a cylinder with constant anisotropic surface impedance $Z_{\varphi\varphi}$ and $Z_{zz} = 0$ must be selected large enough to achieve a distinct contribution from two or more scattering channels. Figure 2(b) provides the design value of the surface impedance required to maximize the scattering cross section of the subwavelength scatterer. In theory, this surface impedance can be of any origin. In practice, it can be realized by corrugating the surface of a metallic rod.

Figure 2(c) depicts the normalized absolute value of $Z_{\varphi\varphi}$ [see Eq. (6)] as a function of corrugation parameters ε, w/p, d, and R. Since $d < R$, Fig. 2(c) indicates a lower limit on permittivity ε, which provides the desired impedance $Z_{\varphi\varphi}$ for a cylindrical superscatterer of radius R. It is evident that this limit generally increases as R decreases. In Fig. 2(c) one can distinguish a number of extrema of $Z_{\varphi\varphi}$. This suggests that a single corrugated metasurface may enhance scattering from the desired cylinder at several frequencies as does a multilayered coating [13,17]. As Fig. 2(a) illustrates, for such frequencies

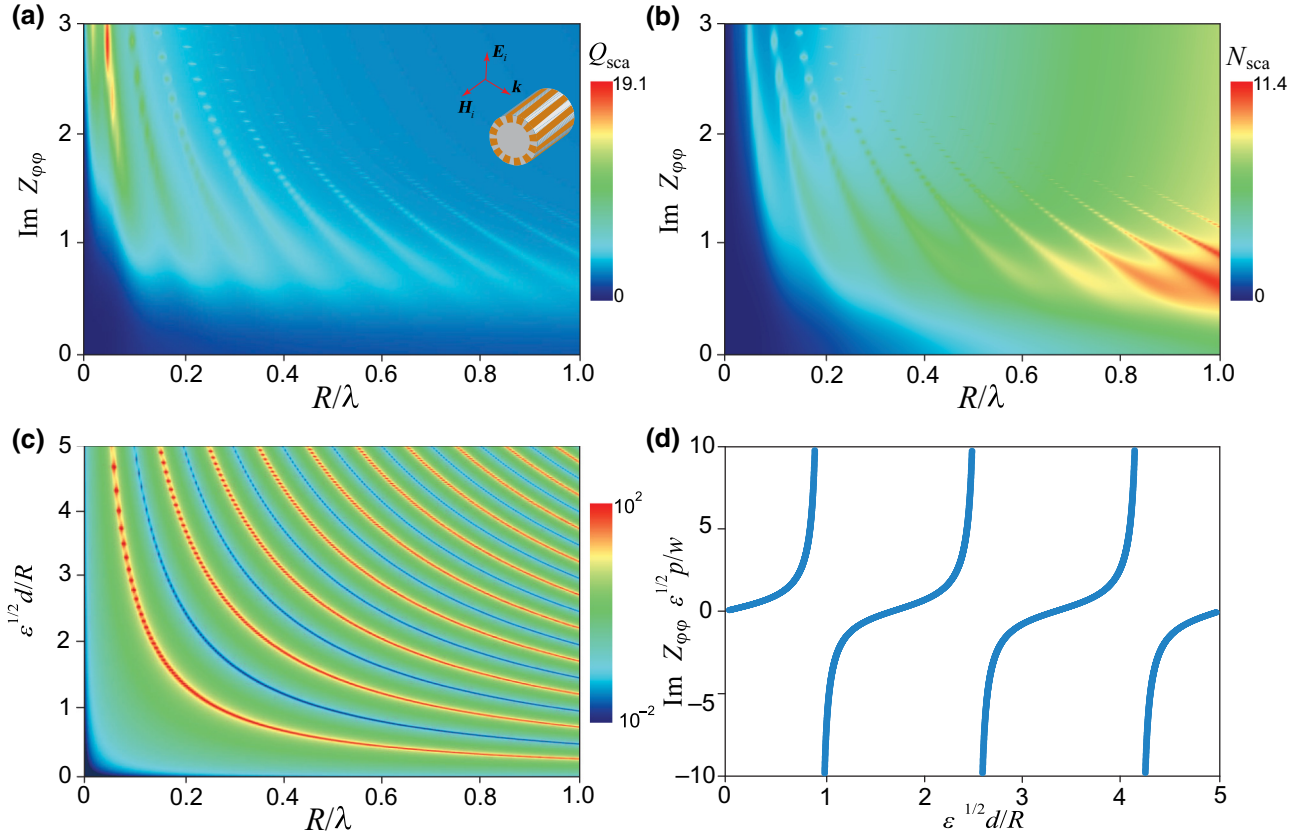

FIG. 2. (a) Scattering efficiency and (b) normalized scattering cross section of a TE_z wave normally incident on a cylinder with radius R and anisotropic surface impedance $Z_{\varphi\varphi}$ and $Z_{zz} = 0$ and (c) absolute value and (d) imaginary part ($R/\lambda = 0.3$) of the normalized surface impedance $Z_{\varphi\varphi}\sqrt{\varepsilon}p/w$ versus corrugation parameters.

$Z_{\varphi\varphi}$ should be near the peak values shown in Fig. 2(c). At these peak values, the surface impedance $Z_{\varphi\varphi}$ changes sign [Fig. 2(d)]. Thus, longitudinal wedge-shaped corrugations can provide both positive and negative values of $\mathrm{Im}\, Z_{\varphi\varphi}$. From Fig. 2(d) one can see that the greater is the design value of the surface impedance, the closer should be the fabrication tolerances for corrugations. It is also clear that it is necessary to keep the permittivity ε of the corrugations as low as possible to alleviate this technological constraint. Our simulations additionally show that wave scattering from a corrugated cylinder is slightly sensitive to the loss tangent ($\tan\delta$) of dielectrics, provided that ε is low. As indicated in Figs. 2(c) and 2(d), the lower is the permittivity ε, the larger are the ratios d/R and w/p required to attain the high averaged impedance $Z_{\varphi\varphi}$ of a corrugated surface. In our simulations, we set the width-to-period ratio w/p of corrugations to 0.9, unless otherwise stated.

In these simulations, for definiteness the frequency of the microwave scatterers of different radii is taken to be the same and is 5 GHz. This frequency is called the "operating frequency." Figure 2(c) indicates the required corrugation parameter values that maximize both Q_{sca} [Fig. 2(a)] and N_{sca} [Fig. 2(b)] for the subwavelength cylinder at the operating frequency. For $R = 0.5$ cm ($R/\lambda \approx 0.08$) the resultant scattering cross section N_{sca} versus frequency is shown in Fig. 3(a). In this case, the permittivity ε of the corrugations is set to 22. Such permittivity is typical of low-loss ($\tan\delta \leq 0.005$) ceramics used in designing microwave metasurfaces [42–44]. From Fig. 3(a) one can see that for the operating frequency the scattering cross sections from the $n = 0$ and $n = \pm 1$ channels are close to the single-channel limit and therefore result in enhanced wave scattering (superscattering). An important point is that this effect is robust to dielectric losses, as opposed to superscattering induced by $n = 0$ and $n = \pm 2$ channels for a nearby frequency of 5.2 GHz. As a result, even with losses, for the operating frequency the scattering cross section of the corrugated cylinder is more than 20 times larger than that of the PEC rod of the same radius $R =$ 0.5 cm. Moreover, as noted above, corrugations may provide multifrequency superscattering from a cylinder. This phenomenon is also clearly seen from Fig. 3(a), which demonstrates scattering enhancement simultaneously for frequencies of 5 and 12.5 GHz. For 12.5 GHz, the superscattering comes from interference of azimuth modes with $n = \pm 1$ and $n = \pm 2$.

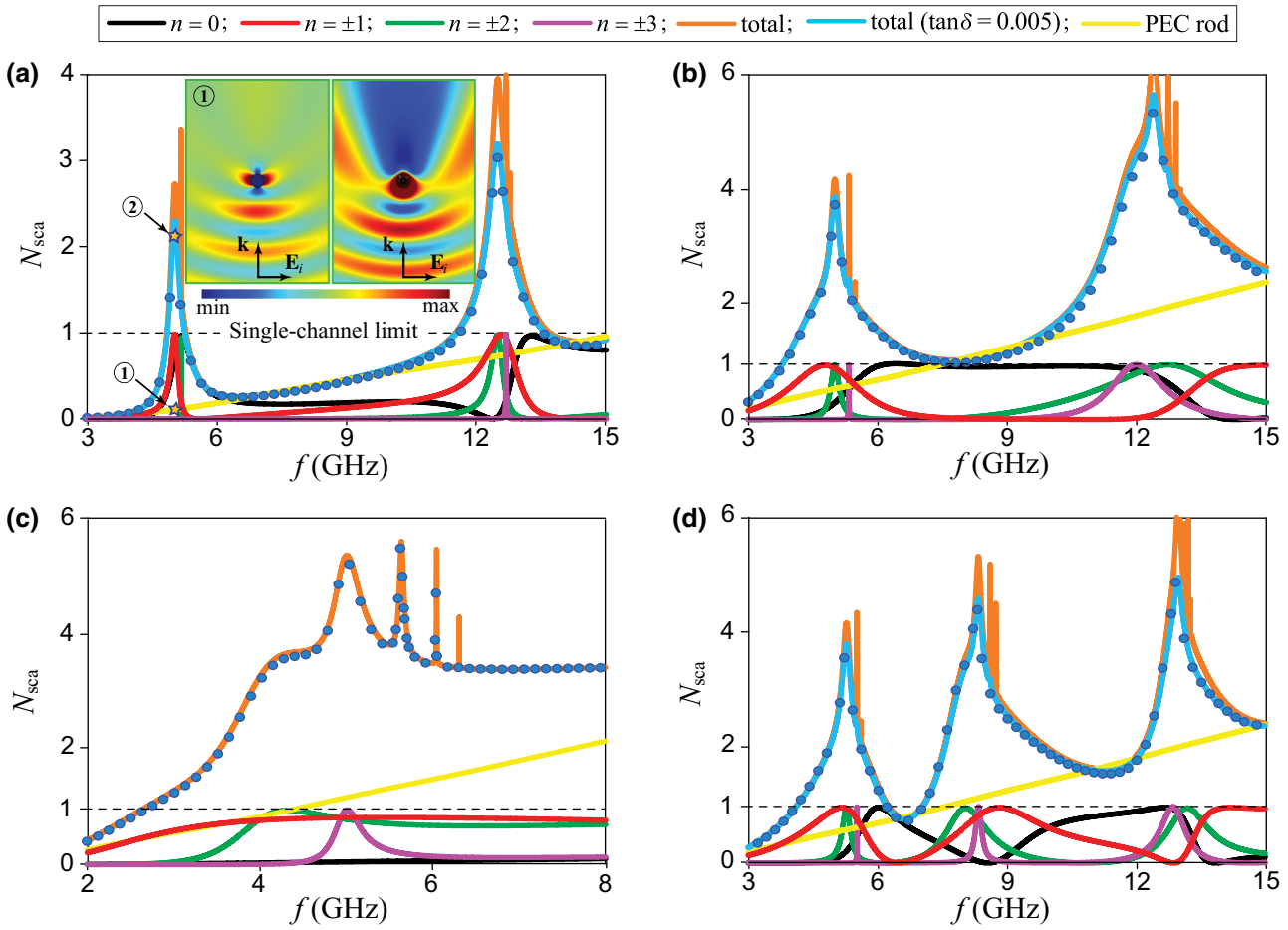

FIG. 3. Total and partial scattering cross sections of a TE_z wave versus frequency for a corrugated cylinder with (a) $R = 0.5$ cm, $d = 0.39$ cm, and $\varepsilon = 22$, (b) $R = 1.0$ cm, $d = 0.92$ cm, and $\varepsilon = 4$, and (c) $R = d = 1.61$ cm and $\varepsilon = 1$. The case in (d) corresponds to wave scattering from a cylinder of radius $R = 1$ cm with two distinctly sized corrugations per period p, each characterized by the same values of $w/p = 0.45$ and $\varepsilon = 4$ and different depths of 0.92 and 0.46 cm. The scattering cross section of the PEC rod of the corresponding radius is shown by the yellow line and the results of full-wave simulations are indicated by circles.

A similar situation occurs for a cylinder of larger radius $R = 1$ cm ($R/\lambda \approx 0.17$). In this case, the permittivity ε of the corrugations can be reduced to 4 (e.g., as for an epoxy resin). As Fig. 3(b) illustrates, such permittivity ensures superscattering from the cylinder for the operating frequency of 5 GHz and a higher frequency of 12.4 GHz as a result of resonance overlap for modes with indices $n = \pm 1, \pm 2$ and $n = 0, \pm 2, \pm 3$, respectively. From comparison of Figs. 3(a) and 3(b), one can see that, along with robustness to material losses, low-index dielectrics benefit from wideband superscattering. In particular, Fig. 3(b) demonstrates enhanced scattering from a PEC rod with relative bandwidth in excess of 120% with respect to the operating frequency.

More importantly, superscattering from a corrugated cylinder can be achieved without use of dielectrics. This is shown in Fig. 3(c), which demonstrates the results for an all-metal superscatterer. Such an all-metal superscatterer is relatively light in weight, since its geometrical transverse cross section is smaller than that of a metal rod of the same radius.

It is also worth noting that multifrequency superscattering from a corrugated cylinder is not a particular problem. It can be easily resolved by filling neighboring corrugations with different dielectrics. Alternatively, this can be done by introducing two or more distinctly sized corrugations within one period p of the structure. Figure 3(d) shows this, as an example, for a doubly corrugated cylinder of radius $R = 1$ cm.

The phenomenon of superscattering from a corrugated cylinder is validated against full-wave simulations by the RF Module of the COMSOL MULTIPHYSICS solver. In simulations, the corrugation period p is taken to satisfy the condition $p/\lambda < 0.03$ and thus is small enough to avoid coupling of spatial harmonics due to corrugations [45]. The results of full-wave simulations are shown in Fig. 3 by markers and agree closely with our analytical findings. The patterns of the electric near field ($|\mathbf{E}|^2$), which

are plotted in the insets in Fig. 3(a) for corrugated and smooth rods at the operating frequency, serve as additional evidence in favor of enhanced scattering of TE_z waves from a PEC cylinder with longitudinal wedge-shaped corrugations.

III. ENHANCED AND REDUCED SCATTERING OF TM_z WAVES

To enhance scattering of TM_z waves ($Q = -1$) from a PEC cylinder, we now turn our attention to transverse ($\mathbf{i}_\parallel \parallel \mathbf{i}_\varphi$) ring-shaped corrugations characterized by the averaged surface impedance with a nonzero component:

$$Z_{zz} = \frac{w}{p}\frac{ik_\perp}{\varepsilon k}\frac{J_n(k_\perp R) - CN_n(k_\perp R)}{J_n'(k_\perp R) - CN_n'(k_\perp R)}, \tag{7}$$

where $C = J_n(k_\perp R_d)/N_n(k_\perp R_d)$ [see Eq. (A10) in the Appendix].

Figures 4(a) and 4(b) show the scattering efficiency and normalized scattering cross section of a subwavelength cylinder versus radius R and constant (mode-independent) surface impedance Z_{zz}. Again, one can see that impedance cylinders of smaller radii scatter waves more efficiently than the PEC rods ($Z_{zz} = Z_{\varphi\varphi} = 0$), but at the same time should be large enough to overcome the singe-channel scattering limit. As seen from Figs. 4(a) and 4(b), the imaginary part of the surface impedance must be negative to enhance scattering of TM_z waves from the cylinder. Such values of Z_{zz} can be provided by corrugations. However, the results shown in Figs. 4(a) and 4(b) should be generally considered as an estimation for a corrugated cylinder. This is because for such a cylinder the surface impedance (7) is not constant, but depends on the azimuth index n.

For different n the dependence of Z_{zz} on the corrugation parameters w/p, ε, d, and R has much in common with that shown in Fig. 2(c) for $Z_{\varphi\varphi}$. However, the larger the ratio d/R, the sharper is the distinction between the values of Z_{zz} for different n. This distinction can be clearly seen from Fig. 4(c) in the case of $d/R = 0.5$ and $R/\lambda = 0.3$. By contrast, for small d/R the impedance Z_{zz} depends only slightly on n. An illustrative example is given in Fig. 4(d) for $d/R = 0.1$ and $R/\lambda = 0.3$. In this case, for low-order modes, Z_{zz} in Eq. (7) behaves like a constant surface impedance.

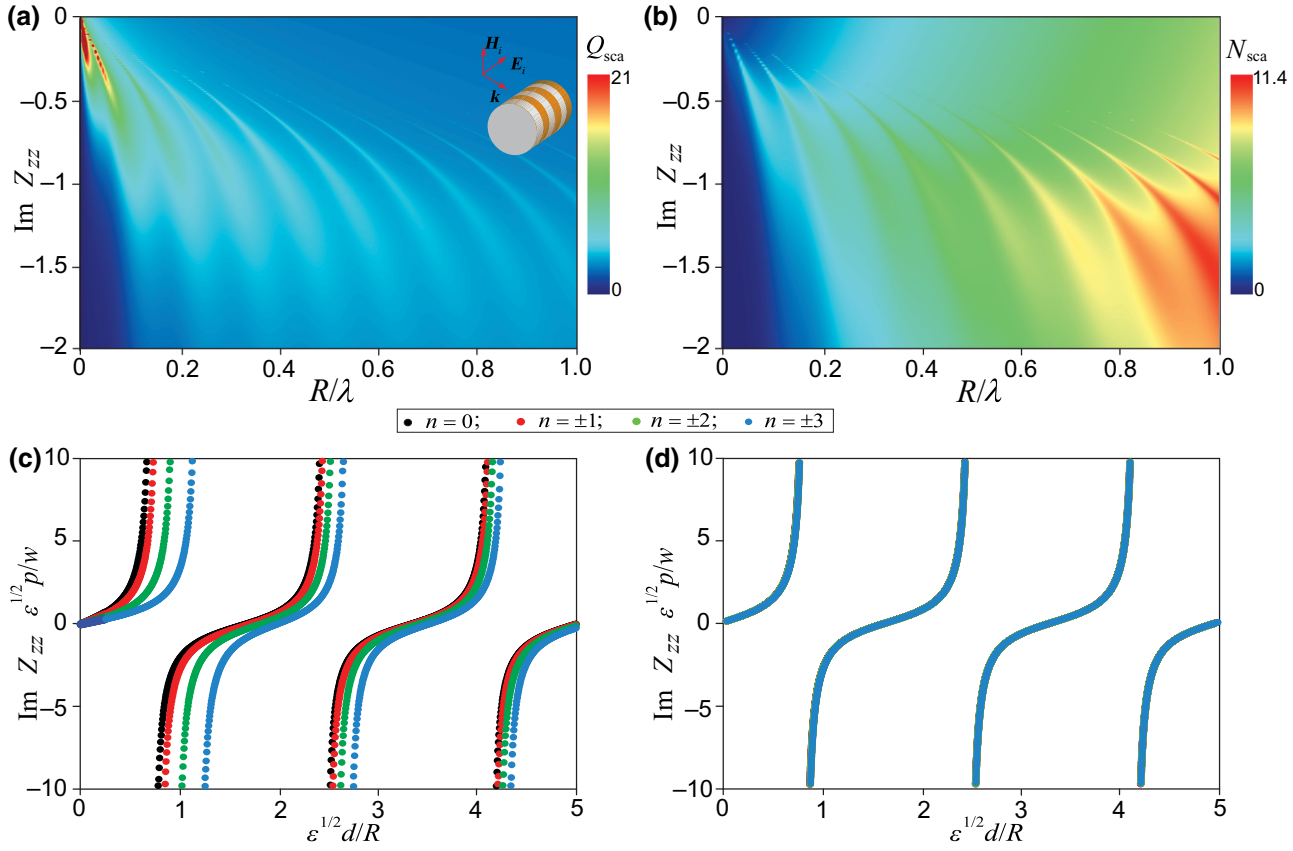

FIG. 4. (a) Scattering efficiency and (b) normalized scattering cross section of a TM_z wave normally incident on a cylinder with radius R and anisotropic surface impedance $Z_{\varphi\varphi} = 0$ and Z_{zz}, and imaginary part of the normalized surface impedance $Z_{zz}\sqrt{\varepsilon}p/w$ as a function of azimuth index n and parameters of a corrugated cylinder with $R/\lambda = 0.3$ for (c) $d/R = 0.5$ and (d) $d/R = 0.1$.

In simulations, for cylinders of radius 0.5 and 1.0 cm we set $w/p = 0.9$ and $\varepsilon = 22$ and then optimize the corrugation depth so as to maximize the scattering cross section of a TM_z wave at the operating frequency of 5 GHz. The resulting dependence of the scattering cross section N_{sca} on frequency is shown in Figs. 5(a) and 5(b). As in the case of TE_z waves, constructive interference of two or more scattering modes results in multifrequency superscattering of TM_z waves from a corrugated cylinder. It is remarkable that for the operating frequency this effect is only slightly affected by dielectric losses, as indicated by Figs. 5(a) and 5(b).

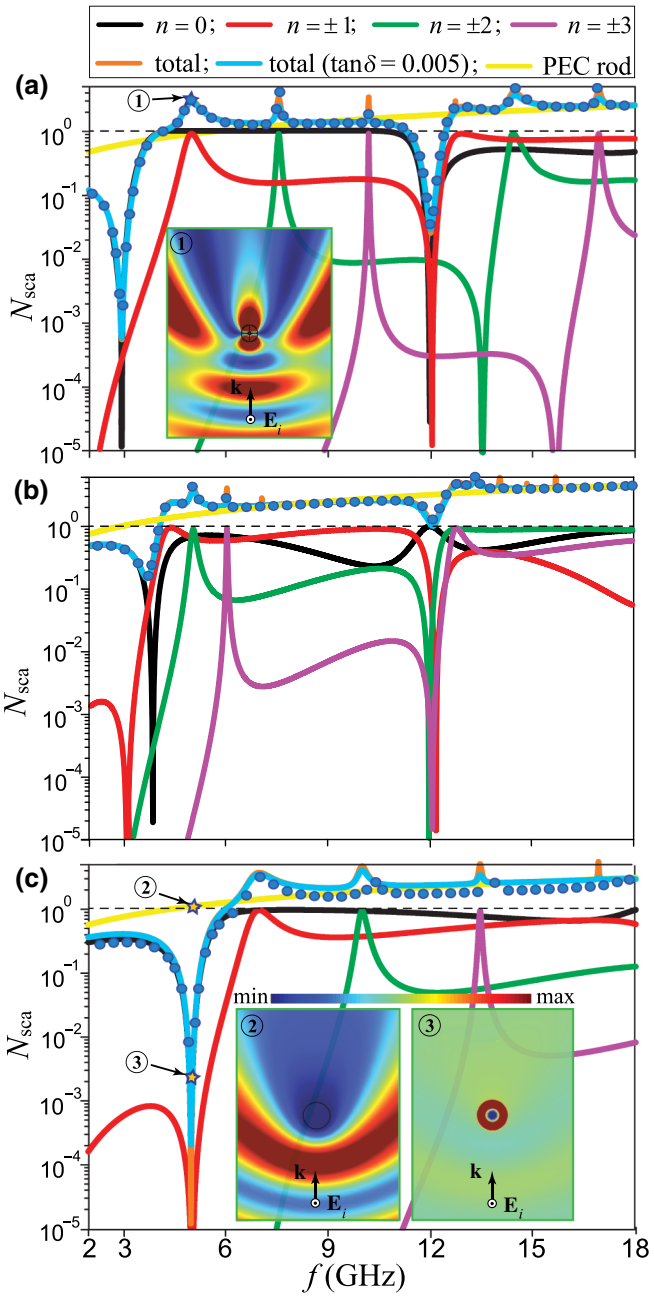

FIG. 5. Total and partial scattering cross sections of a TM_z wave versus frequency for a corrugated cylinder with (a) $R = 0.5$ cm, $d = 0.4$ cm, and $\varepsilon = 22$, (b) $R = 1.0$ cm, $d = 0.4$ cm, and $\varepsilon = 22$, and (c) $R = 0.5$ cm, $d = 0.36$ cm, $w/p = 0.47$, and $\varepsilon = 11$, along with results for PEC rods of the same radii (yellow lines) and data from full-wave simulations (circles).

Although our investigation is concerned mainly with the phenomenon of superscattering, we also reveal that transverse corrugations may additionally provide cloaking of a subwavelength PEC cylinder for incident TM_z waves. A similar effect of reduced and enhanced scattering from a single structure was reported in Refs. [11] and [28] for a core-shell plasmonic nanowire and sphere (see Fig. 6 in Ref. [28]), respectively. For the corrugated cylinder of radius 0.5 cm, the reduced scattering can be seen from Fig. 5(a). It is notable that in this case cylinder cloaking by corrugations occurs simultaneously for two frequencies close to 3 and 12 GHz. Thus, the PEC cylinder with transverse ring-shaped corrugations possesses a unique feature of both cloaking and superscattering at multiple frequencies. For the operating frequency of 5 GHz, the reduced scattering from a cylinder can be achieved by optimization of corrugation parameters. In the case of $R = 0.5$ cm, the results of such optimization are shown in Fig. 5(c). It can be seen that in this case highly efficient cloaking of a cylindrical scatterer occurs owing to simultaneous suppression of the fundamental ($n = 0$) and first ($n = \pm 1$) scattering modes by corrugations. Thus, surface corrugation is a suitable cloaking technique for metallic cylinders.

The cloaking ability distinguishes the transverse corrugations from the longitudinal ones. This is because the cloaking condition $U_n = 0$ requires the surface impedance of a cylinder to be equal to $\mathrm{Im}\, Z_{\varphi\varphi} = i\lambda_1$ and $\mathrm{Im}\, Z_{zz} = i(\varepsilon_2\lambda_1)^{-1}$ for normally incident TE_z and TM_z waves, respectively. For a deep-subwavelength cylinder ($k_2R \ll 1$) one has $i\sqrt{\varepsilon_2}\lambda_1 \approx k_2R/(2|n|+2) - |n|/(k_2R)$. Obviously, in this case, the surface impedance of a cylinder must have opposite signs for $n = 0$ and $|n| = 1$ to ensure suppression of the two lowest-order azimuth modes. Such a situation is possible for TM_z waves normally incident on a transversely corrugated cylinder [see, e.g., Fig. 5(c)] but cannot be achieved with the longitudinal wedge-shaped corrugations characterized by constant (mode-independent) surface impedance (6).

As Fig. 5 indicates, our simple analytical approach is in good agreement with full-wave simulations and therefore is particularly suitable for fast and accurate design of corrugated cylindrical scatterers. From Fig. 5 it is apparent that subwavelength corrugations offer considerable scope for manipulation of wave scattering. This can also be seen from the near-field structure of the TM_z wave in the insets in Figs. 5(a) and 5(c), which show both superscattering and cloaking properties for corrugated cylinders of identical radius at the operating frequency.

IV. ALL-METAL SUPERSCATTERER

Recent experimental observations reported superscattering for TM_z waves [17]. Here, the purpose is to demonstrate the same phenomenon for TE_z waves. For this purpose, we use a simple design solution in the form of an all-metal superscatterer. Two prototypes of the superscatterer are designed and fabricated. For sample preparation, cylindrical copper billets with a diameter of 3 cm and a length of 40 cm are used. Longitudinal wedge-shaped corrugations are engraved on the billets with use of a precise milling machine. The design parameters of the corrugations of the first (second) scatterers are as follows: $N = 36$ ($N = 41$), $w = 0.15$ cm ($w = 0.65$ cm), and $d = 0.7$ cm ($d = 0.5$ cm). According to our analytical estimations, these parameters ensure operating frequencies of about 8.46 GHz ($R/\lambda \approx 0.42$) and 10.68 GHz ($R/\lambda \approx 0.52$) for the all-metal superscatterers with $N = 36$ and $N = 41$, respectively. These frequencies are within the frequency range from 3 to 15 GHz, which is covered by our experimental facilities.

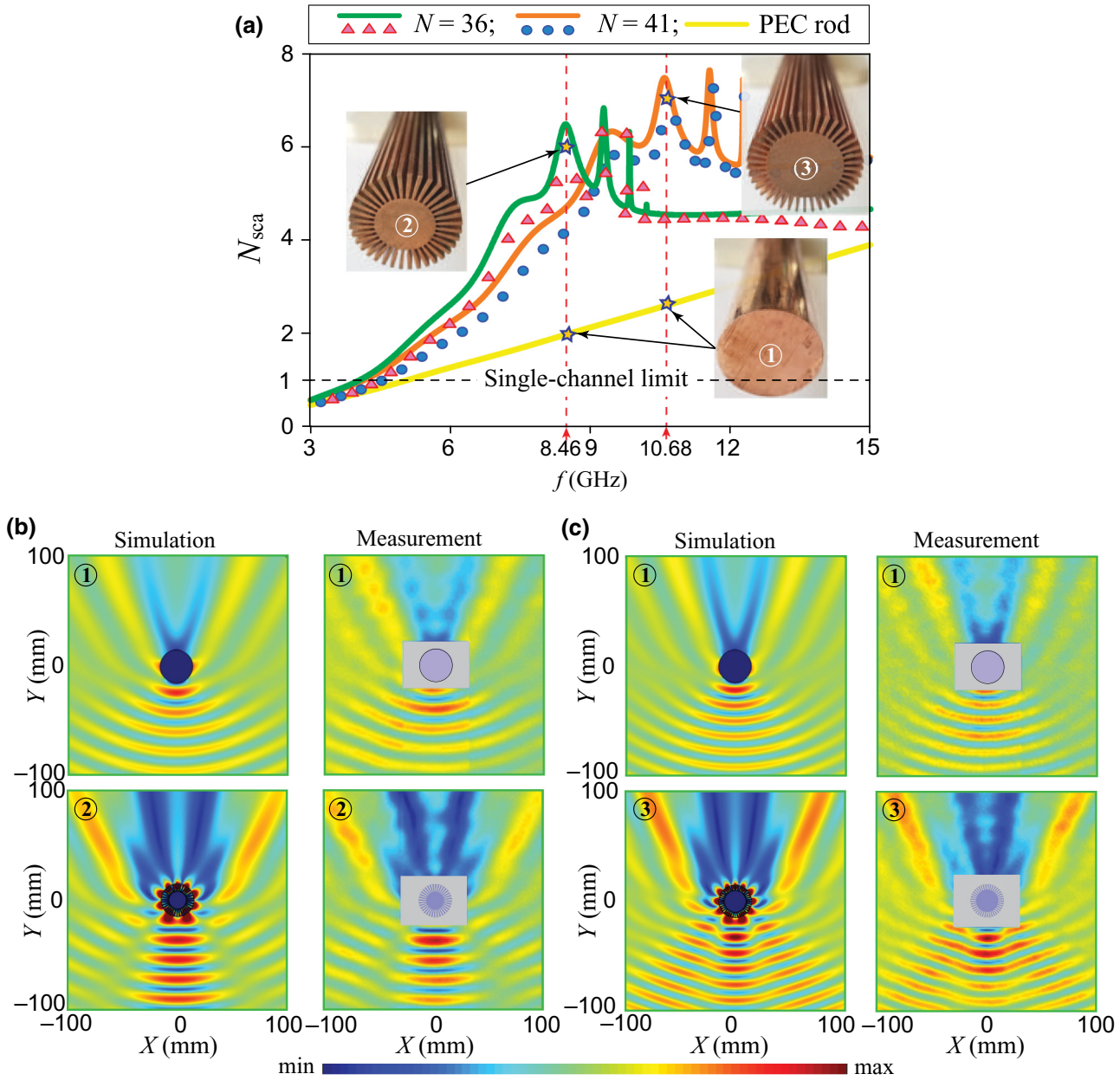

FIG. 6. (a) Theoretical (lines) and simulated (circles and triangles) frequency dependence of scattering cross sections of the TE_z wave for a reference copper rod and two designed corrugated cylinders with $N = 36$ and $N = 41$, and patterns of the scattered electric near field ($|E_x|$) simulated and measured at frequencies of (b) 8.46 GHz and (c) 10.68 GHz. In the cases for (b),(c), the plane waves come from the bottom side and propagate along the y axis.

Figure 6(a) shows theoretical and simulation results for the scattering cross sections of the designed scatterers in the frequency range chosen. As seen from Fig. 6(a), there is some distinction between the theory and the full-wave simulations. This is explained by coupling between azimuth spatial harmonics due to corrugations. This coupling is ignored in our theoretical model (see the Appendix) and increases in importance with increasing period of the corrugations [45]. For the operating frequencies of the designed superscatterers with 36 and 41 corrugations, the ratio p/λ is relatively large and approximately equal to 0.07 and 0.08, respectively. Despite this, for these frequencies our simple and fast theoretical approach still gives fairly accurate results.

To observe the superscattering from a corrugated cylinder, the experimental sample is placed in an anechoic chamber. The sample is fixed vertically at a distance of 1.5 m from a rectangular broadband horn antenna (HengDa Microwave HD-10180DRHA10SZJ). The antenna is connected to the first port of a Rohde & Schwarz ZVA50 vector network analyzer. The antenna generates a linearly polarized quasi-plane-wave whose polarization is orthogonal to the symmetry axis (the z axis) of the sample.

An electrically small dipole probe is positioned at the half height of the vertically standing scatterer and oriented along the polarization direction of the incident wave. The probe detects the dominant component (E_x) of the scattered electric near field and is connected to the second port of the vector network analyzer. A LINBOU near-field imaging system is used for the near-field mapping. The scan area around the sample has dimensions 200×200 mm^2 in the x-y plane. In the measurements, the probe automatically moves in the scan area with a 2-mm step along two orthogonal directions. At each probe position, both the amplitude and the phase of the scattered electric field are measured. The exception is the area near the sample with dimensions 60×44 mm^2. This area is experimentally inaccessible because of the technical limitation on the distance between the moving probe and the vertically standing sample.

Figures 6(b) and 6(c) show the simulated and measured scattered-electric-near-field patterns ($|E_x|$) for a reference copper rod of diameter 3 cm (upper row) and two samples of the all-metal superscatterer (bottom row) at the operating frequencies. It can be seen that the measurements are in reasonable agreement with the simulations and indeed demonstrate the enhanced scattering of the TE$_z$ wave from the corrugated cylinder. These measurements present experimental evidence of superscattering for all-metal cylindrical objects. It should be noted that the designed scatterers have relatively large transverse cross sections. Therefore, they are characterized by a lower scattering efficiency in comparison with smaller scatterers [see, e.g., Fig. 3(a)]. The size of the superscatterer can be reduced by filling the corrugations with a dielectric. In practice, however, this adds complexity to the design and therefore calls for advanced fabrication techniques.

V. CONCLUSIONS

It is common knowledge that surface impedance offers a means for manipulating wave scattering from subwavelength objects. In this regard, tensor impedance surfaces have the broadest potential for application, but are now rare in practice because of the lack of feasible design solutions, especially in nonplanar geometries. It is shown that a metallic rod with helical periodic corrugations is a concrete example of a cylindrical scatterer with a tensor impedance surface. Explicit expressions are derived for the amplitudes of arbitrarily polarized plane waves scattered from such a cylinder. Particular attention is given to the surface impedance, which enhances wave scattering from the cylinder, but induces no polarization conversion of the incident wave. For TE$_z$ and TM$_z$ incident waves, the required surface impedance of a subwavelength cylinder can be provided by longitudinal and transverse dielectric-filled corrugations, respectively.

It is demonstrated that such corrugations, when properly designed, initiate superscattering of waves; that is, they ensure resonance overlap for two or more scattering modes (channels). This theoretical finding is validated against full-wave simulations. The superscattering from a subwavelength corrugated cylinder occurs at multiple frequencies, which can be broadly tuned or even increased in number by adjustment of the corrugation parameters. This phenomenon is found to be robust to material losses and tolerances of corrugation fabrication, provided that the permittivity of the corrugation filling is not too high. It is shown that in this case enhanced scattering of TE$_z$ waves from a cylinder features a broad frequency bandwidth in excess of 100% with respect to the operating frequency.

The broadest bandwidth of enhanced scattering can be achieved for hollow corrugations. In this case, the subwavelength corrugated cylinder behaves as a broadband all-metal superscatterer of TE$_z$ waves. Two experimental samples of such superscatterers of the same radius are designed and fabricated to operate at distinct frequencies. In the microwave band, superscattering from these samples is demonstrated by measurement of the electric near field, which provides experimental evidence of this phenomenon for all-metal objects.

It is shown that superscattering of TM$_z$ waves from a corrugated cylinder looks somewhat similar to that for TE$_z$ waves. But, in addition to this effect, the corrugations are found to be responsible for cloaking of the cylinder for incident TM$_z$ waves. Efficient cloaking of a subwavelength cylinder is demonstrated as a result of simultaneous suppression of the two lowest-order scattering modes. Besides, a corrugated cylinder can be designed to exhibit cloaking at multiple frequencies. The unique feature of

both multifrequency superscattering and multifrequency cloaking makes this scatterer particularly attractive for use in sensor and antenna applications.

ACKNOWLEDGMENT

The authors are grateful for support from Jilin University, China.

Note added.—Recently, two related papers devoted to superscattering appeared. In the first paper [46], a solid mazelike structure is proposed and experimentally realized to achieve superscattering of sound. In the second paper [47], an electromagnetic superscatterer in the form of a spiral structure is theoretically investigated on the basis of the effective-medium theory [48]. Both these papers deal with two-dimensional scatterers behaving like a corrugated structure. Therefore, the results obtained in Refs. [46,47] can be considered as additional evidence of superscattering induced by subwavelength corrugations and demonstrate growing interest in this phenomenon.

APPENDIX: SUBWAVELENGTH CORRUGATED CYLINDER

Consider subwavelength periodic corrugations that are parallel to the vector $\mathbf{i}_\parallel$ and have period p and width w along the y axis and depth d along the x axis [Figs. 1(b) and 1(c)]. The corrugations are made in perfect electric conductor and are filled with a dielectric of permittivity ε and permeability $\mu = 1$. Under the subwavelength condition, such corrugations do not support waves with nonzero component $E_\parallel$ of the electric field [22–25,49–53]. Thus, on the top (aperture) of the corrugations one has the boundary condition $E_\parallel = 0$, which is identical to that provided by a PEC surface $x = R$. By contrast, inside the corrugations there are modes with nonzero electric field component E_y. Among them, the fundamental mode with a uniform field distribution along the y axis is dominant for $w < p \ll \lambda$ and has the following field structure: $\{\mathbf{E}, \mathbf{H}\} = \{\mathbf{E}(x), \mathbf{H}(x)\} \exp(-i\omega t + ik_\parallel x_\parallel)$, where ω and $\lambda = 2\pi c/\omega$ are the mode frequency and wavelength, respectively, and $x_\parallel$ and $k_\parallel$ are the coordinate and wave number along $\mathbf{i}_\parallel$, respectively. For this mode E_y and $H_\parallel$ are related to each other by the expression

$$E_y = -\frac{ik}{k_\perp^2}\frac{dH_\parallel}{dx}, \tag{A1}$$

where $k_\perp^2 = \varepsilon k^2 - k_\parallel^2 \approx \varepsilon k^2$ and the condition $k_\parallel^2 \ll \varepsilon k^2$ is assumed to be fulfilled.

First, we consider rectangular corrugations [Fig. 1(b)]. For the fundamental mode of such corrugations one has the following solution of the wave equation:

$$H_\parallel = A\cos[k_\perp(x - R_d)], \tag{A2}$$

which satisfies the PEC boundary condition on the bottom and side surfaces of corrugations for any unknown constant A.

Using Eqs. (A1) and (A2), one can readily obtain the surface impedance along the corrugation width for $x = R$:

$$W = \frac{E_y}{H_\parallel} = \frac{ik}{k_\perp}\tan k_\perp d. \tag{A3}$$

Outside the corrugation aperture the condition $E_y/H_\parallel = 0$ holds true on the PEC surface $x = R$. The averaged boundary condition for the entire surface $x = R$ can be obtained by combining this condition with Eq. (A3) and $E_\parallel(R) = 0$:

$$E_y = Z_\perp H_\parallel, \quad E_\parallel = -Z_\parallel H_y, \tag{A4}$$

where $Z_\perp = \langle E_y/H_\parallel\rangle = w/pW$ and $Z_\parallel = \langle E_\parallel/H_y\rangle = 0$ are the principal components of the surface impedance tensor

$$\hat{\mathbf{Z}} = \begin{pmatrix} Z_\perp & 0 \\ 0 & Z_\parallel \end{pmatrix}, \tag{A5}$$

and angle brackets $\langle\ldots\rangle$ denote averaging over $x = R$. The result obtained, if necessary, can be generalized to account for finite conductivity of metallic corrugations [45,54,55]. For good conductors the problem of wave attenuation due to Ohmic losses is of no concern in the microwave band, but gains in importance for subterahertz and terahertz frequencies [45,54–56].

We now assume that the plane $x = r = R$ coincides with the surface of a cylindrical scatterer and orthogonal unit vectors $\mathbf{i}_z$ and $\mathbf{i}_\varphi$ of the cylindrical coordinate system are rotated by angle θ with respect to the $\mathbf{i}_\parallel$ and $\mathbf{i}_y$ pair [Fig. 1(a)]. In the coordinates $\{r, \varphi, z\}$, the surface impedance tensor (A5) is generally nondiagonal

$$\hat{\mathbf{Z}} = \begin{pmatrix} Z_{\varphi\varphi} & Z_{\varphi z} \\ Z_{z\varphi} & Z_{zz} \end{pmatrix}, \tag{A6}$$

and the boundary conditions on the cylinder surface $r = R$ (metasurface) take the form of Eq. (2), where $Z_{\varphi\varphi} = Z_\perp\cos^2\theta + Z_\parallel\sin^2\theta$, $Z_{zz} = Z_\parallel\cos^2\theta + Z_\perp\sin^2\theta$, and $Z_{\varphi z} = Z_{z\varphi} = (Z_\parallel - Z_\perp)\sin\theta\cos\theta$.

Tensor (A6) describes the averaged surface impedance for a metallic cylinder with helical subwavelength corrugations. It takes the well-known diagonal form in the extreme cases of $\theta = 0^\circ$ and $\theta = 90^\circ$, which correspond to a PEC cylinder with longitudinal [50,51,54,55] and transverse [22,24,50] rectangular corrugations, respectively.

In the derivation of Eq. (A6) we proceed from two assumptions. The first one is that the condition $k_\parallel^2 \ll \varepsilon k^2$ is

true, where $k_\parallel^2 = (k_z \cos\theta + nR^{-1}\sin\theta)^2$ [32,55]. For normal wave incidence the axial wave number k_z is 0, and this condition reduces to the limitation $|n|\sin\theta \ll 2\pi\sqrt{\varepsilon}R/\lambda$ on the azimuth index n of modes in Eq. (1). Simple estimation shows that, even with $\theta = 90°$, $\varepsilon = 1$, and $R/\lambda \approx 1$, the first assumption in use is good for low azimuth harmonics with $n = 0, \pm 1, \pm 2$.

The second widely accepted assumption implies that the cylinder incorporates corrugations of rectangular shape [24,51,57]. This simplification takes no account of the cylinder curvature and is good for sufficiently large values of $k_\perp R_d$ (e.g., for large ε). One can avoid it in two practical cases. The first one is a metallic cylinder with longitudinal ($\theta = 0°$) wedge-shaped corrugations [23,49,50,52]. In this case [Fig. 1(c)], substitution of

$$H_\parallel = H_z = A_1\left[J_0(k_\perp x) - BN_0(k_\perp x)\right] \tag{A7}$$

into Eq. (A3) gives

$$Z_{\varphi\varphi} = -\frac{w}{p}\frac{ik}{k_\perp}\frac{J_0'(k_\perp R) - BN_0'(k_\perp R)}{J_0(k_\perp R) - BN_0(k_\perp R)}, \quad Z_{zz} = 0, \tag{A8}$$

where $B = J_0'(k_\perp R_d)/N_0'(k_\perp R_d)$, where $R_d = R - d$. Such anisotropic surface impedance has an effect on TE_z waves [58].

The second case is a cylinder with transverse ($\theta = 90°$) ring-shaped corrugations [20–22,25,50,52], which affect normally incident TM_z waves [58]. In this case, using the field expressions

$$E_z = A_2\left[J_n(k_\perp r) - CN_n(k_\perp r)\right], \quad H_\varphi = \frac{i\varepsilon k}{k_\perp^2}\frac{dE_z}{dr}, \tag{A9}$$

one obtains

$$Z_{\varphi\varphi} = 0, \quad Z_{zz} = \frac{w}{p}\frac{ik_\perp}{\varepsilon k}\frac{J_n(k_\perp R) - CN_n(k_\perp R)}{J_n'(k_\perp R) - CN_n'(k_\perp R)}, \tag{A10}$$

where $C = J_n(k_\perp R_d)/N_n(k_\perp R_d)$. It is noteworthy that Eq. (A10) depends on the azimuth index n. A similar situation holds for a dielectric cylinder coated by transverse (circumferential) [59] or helical [32,36] conducting strips, as well as for a dielectric-lined metallic cylinder and multilayered-dielectric cylindrical structures [50,60].

[1] D. Vercruysse, Y. Sonnefraud, N. Verellen, F. B. Fuchs, G. Di Martino, L. Lagae, V. V. Moshchalkov, S. A. Maier, and P. Van Dorpe, Unidirectional side scattering of light by a single-element nanoantenna, Nano Lett. **13**, 3843 (2013).

[2] B. Ng, J. Wu, S. M. Hanham, A. I. Fernández-Domínguez, N. Klein, Y. F. Liew, M. B. H. Breese, M. Hong, and S. A. Maier, Spoof plasmon surfaces: A novel platform for THz sensing, Adv. Opt. Mater. **1**, 543 (2013).

[3] S. Zeng, D. Baillargeat, H.-P. Ho, and K.-T. Yong, Nanomaterials enhanced surface plasmon resonance for biological and chemical sensing applications, Chem. Soc. Rev. **43**, 3426 (2014).

[4] J. G. Smith, J. A. Faucheaux, and P. K. Jain, Plasmon resonances for solar energy harvesting: A mechanistic outlook, Nano Today **10**, 67 (2015).

[5] Y. Zhang, L. Zhou, J.-Q. Li, Q.-J. Wang, and C.-P. Huang, Ultra-broadband and strongly enhanced diffraction with metasurfaces, Sci. Rep. **5**, 10119 (2015).

[6] Z. Han, Y. Zhang, and S. I. Bozhevolnyi, Spoof surface plasmon-based stripe antennas with extreme field enhancement in the terahertz regime, Opt. Lett. **40**, 2533 (2015).

[7] B. Gholipour, G. Adamo, D. Cortecchia, H. N. S. Krishnamoorthy, M. D. Birowosuto, N. I. Zheludev, and C. Soci, Organometallic perovskite metasurfaces, Adv. Mater. **29**, 1604268 (2017).

[8] A. Alù and N. Engheta, Polarizabilities and effective parameters for collections of spherical nanoparticles formed by pairs of concentric double-negative, single-negative, and/or double-positive metamaterial layers, J. Appl. Phys. **97**, 094310 (2005).

[9] Z. Ruan and S. Fan, Superscattering of Light From Subwavelength Nanostructures, Phys. Rev. Lett. **105**, 013901 (2010).

[10] Z. Ruan and S. Fan, Design of subwavelength superscattering nanospheres, Appl. Phys. Lett. **98**, 043101 (2011).

[11] A. Mirzaei, I. V. Shadrivov, A. E. Miroshnichenko, and Y. S. Kivshar, Cloaking and enhanced scattering of core-shell plasmonic nanowires, Opt. Express **21**, 10454 (2013).

[12] R. Li, B. Zheng, X. Lin, R. Hao, S. Lin, W. Yin, E. Li, and H. Chen, Design of ultracompact graphene-based superscatterers, IEEE J. Sel. Top. Quantum Electron. **23**, 130 (2016).

[13] H. S. Raad, C. J. Zapata-Rodríguez, and Z. Atlasbaf, Multifrequency super-scattering from sub-wavelength graphene-coated nanotubes, J. Opt. Soc. Am. B **36**, 2292 (2019).

[14] C. Qian, X. Lin, Y. Yang, F. Gao, Y. Shen, J. Lopez, I. Kaminer, B. Zhang, E. Li, M. Soljačić, and H. Chen, Multifrequency superscattering from subwavelength hyperbolic structures, ACS Photonics **5**, 1506 (2018).

[15] Y. R. Padooru, A. B. Yakovlev, P.-Y. Chen, and A. Alù, Analytical modeling of conformal mantle cloaks for cylindrical objects using sub-wavelength printed and slotted arrays, J. Appl. Phys. **112**, 034907 (2012).

[16] Y. Ra'di, C. R. Simovski, and S. A. Tretyakov, Thin Perfect Absorbers for Electromagnetic Waves: Theory, Design, and Realizations, Phys. Rev. Appl. **3**, 037001 (2015).

[17] C. Qian, X. Lin, Y. Yang, X. Xiong, H. Wang, E. Li, I. Kaminer, B. Zhang, and H. Chen, Experimental Observation of Superscattering, Phys. Rev. Lett. **122**, 063901 (2019).

[18] A. Mirzaei, A. E. Miroshnichenko, I. V. Shadrivov, and Y. S. Kivshar, Superscattering of light optimized by a genetic algorithm, Appl. Phys. Lett. **105**, 011109 (2014).

[19] W. Liu, Superscattering pattern shaping for radially anisotropic nanowires, Phys. Rev. A **96**, 023854 (2017).

[20] H. E. M. Barlow and A. E. Karbowiak, An experimental investigation of the properties of corrugated cylindrical surface waveguides, Proc. IEE Part III **101**, 182 (1954).

[21] G. Piefke, The transmission characteristics of a corrugated guide, IRE Trans. Antennas Propag. **7**, 183 (1959).

[22] A. F. Harvey, Periodic and guiding structures at microwave frequencies, IRE Trans. Microwave Theory Tech. **8**, 30 (1960).

[23] J. B. Davies, An investigation of some waveguide structures for the propagation of circular TE modes, Proc. IEE Part C **109**, 162 (1962).

[24] B. Z. Katsenelenbaum, *Vysokochastotnaya Elektrodinamika (High Frequency Electrodynamics)* (Nauka, Moscow, 1966).

[25] P. J. B. Clarricoats and P. K. Saha, Theoretical analysis of cylindrical hybrid modes in a corrugated horn, Electron. Lett. **5**, 187 (1969).

[26] *Spoof Surface Plasmon Metamaterials*, edited by P. A. Huidobro, A. I. Fernández-Domínguez, J. B. Pendry, L. Martin-Moreno, and F. J. Garcia-Vidal (Cambridge University Press, Cambridge, 2018).

[27] C. F. Bohren and D. R. Huffman, *Absorption and Scattering of Light by Small Particles* (Wiley, New York, 1998).

[28] A. Alù and N. Engheta, Achieving transparency with plasmonic and metamaterial coatings, Phys. Rev. E **72**, 016623 (2005).

[29] A. Alù, Mantle cloak: Invisibility induced by a surface, Phys. Rev. B **80**, 245115 (2009).

[30] R. Fleury, F. Monticone, and A. Alù, Invisibility and Cloaking: Origins, Present, and Future Perspectives, Phys. Rev. Appl. **4**, 037001 (2015).

[31] V. I. Fesenko, V. I. Shcherbinin, and V. R. Tuz, Multiple invisibility regions induced by symmetry breaking in a trimer of subwavelength graphene-coated nanowires, J. Opt. Soc. Am. A **35**, 1760 (2018).

[32] V. I. Shcherbinin, Y. K. Moskvitina, V. I. Fesenko, and V. R. Tuz, Dual-polarized all-angle cloaking of a dielectric nanowire by helical graphene ribbons, Phys. Rev. B **100**, 035428 (2019).

[33] B. H. Fong, J. S. Colburn, J. J. Ottusch, J. L. Visher, and D. F. Sievenpiper, Scalar and tensor holographic artificial impedance surfaces, IEEE Trans. Antennas Propag. **58**, 3212 (2010).

[34] A. M. Patel and A. Grbic, Effective surface impedance of a printed-circuit tensor impedance surface (PCTIS), IEEE Trans. Microwave Theory Tech. **61**, 1403 (2013).

[35] R. G. Quarfoth and D. F. Sievenpiper, Nonscattering waveguides based on tensor impedance surfaces, IEEE Trans. Antennas Propag. **63**, 1746 (2015).

[36] V. I. Shcherbinin, V. I. Fesenko, and V. R. Tuz, Low-loss forward and backward surface plasmons in a semiconductor nanowire coated by helical graphene strips, J. Opt. Soc. Am. B **35**, 2066 (2018).

[37] M. Selvanayagam and G. V. Eleftheriades, Polarization control using tensor Huygens surfaces, IEEE Trans. Antennas Propag. **62**, 6155 (2014).

[38] S. Wu, S. Xu, T. L. Zinenko, V. V. Yachin, S. L. Prosvirnin, and V. R. Tuz, 3D-printed chiral metasurface as a dichroic dual-band polarization converter, Opt. Lett. **44**, 1056 (2019).

[39] S.-E. Mun, J. Hong, J.-G. Yun, and B. Lee, Broadband circular polarizer for randomly polarized light in few-layer metasurface, Sci. Rep. **9**, 2543 (2019).

[40] M. R. Akram, M. Q. Mehmood, X. Bai, R. Jin, M. Premaratne, and W. Zhu, High efficiency ultrathin transmissive metasurfaces, Adv. Opt. Mater. **7**, 1801628 (2019).

[41] S. Wu, V. V. Yachin, V. I. Shcherbinin, and V. R. Tuz, Chiral metasurfaces formed by 3D-printed square helices: A flexible tool to manipulate wave polarization, J. Appl. Phys. **126**, 103101 (2019).

[42] S. Xu, A. Sayanskiy, A. S. Kupriianov, V. R. Tuz, P. Kapitanova, H.-B. Sun, W. Han, and Y. S. Kivshar, Experimental observation of toroidal dipole modes in all-dielectric metasurfaces, Adv. Opt. Mater. **7**, 1801166 (2019).

[43] A. Sayanskiy, A. S. Kupriianov, S. Xu, P. Kapitanova, V. Dmitriev, V. V. Khardikov, and V. R. Tuz, Controlling high-Q trapped modes in polarization-insensitive all-dielectric metasurfaces, Phys. Rev. B **99**, 085306 (2019).

[44] V. I. Fesenko, A. S. Kupriianov, A. Sayanskiy, V. I. Shcherbinin, A. Trubin, and V. R. Tuz, Approach to analysis of all-dielectric free-form antenna systems, Opt. Express **27**, 22363 (2019).

[45] T. I. Tkachova, V. I. Shcherbinin, and V. I. Tkachenko, Selectivity properties of cylindrical waveguides with longitudinal wall corrugations for second-harmonic gyrotrons, J. Infrared Millim. Terahertz Waves **40**, 1021 (2019).

[46] F. Liu, S. Zhang, L. Luo, W. Li, Z. Wang, and M. Ke, Superscattering of Sound by a Deep-Subwavelength Solid Mazelike Rod, Phys. Rev. Appl. **12**, 064063 (2019).

[47] H.-W. Wu, Y. Fang, J.-Q. Quan, Y.-Z. Han, Y.-Q. Yin, Y. Li, and Z.-Q. Sheng, Multifrequency superscattering with high Q factors from a deep-subwavelength spoof plasmonic structure, Phys. Rev. B **100**, 235443 (2019).

[48] Z. Liao, A. I. Fernández-Domínguez, J. Zhang, S. A. Maier, T. J. Cui, and Y. Luo, Homogenous metamaterial description of localized spoof plasmons in spiral geometries, ACS Photonics **3**, 1768 (2016).

[49] T. Scharten, J. Nellen, and F. van den Bogaart, Longitudinally slotted conical horn antenna with small flare angle, IEE Proc. Part H **128**, 117 (1981).

[50] S. F. Mahmoud, *Electromagnetic Waveguides: Theory and Applications* (IET, London, 1991), Vol. 32.

[51] C. T. Iatrou, S. Kern, and A. B. Pavelyev, Coaxial cavities with corrugated inner conductor for gyrotrons, IEEE Trans. Microwave Theory Tech. **44**, 56 (1996).

[52] J. J. Barroso, R. A. Correa, and P. J. de Castro, Gyrotron coaxial cylindrical resonators with corrugated inner conductor: Theory and experiment, IEEE Trans. Microwave Theory Tech. **46**, 1221 (1998).

[53] S. Tretyakov, *Analytical Modeling in Applied Electromagnetics* (Artech House, Boston, 2003).

[54] V. I. Shcherbinin and V. I. Tkachenko, Cylindrical cavity with distributed longitudinal corrugations for second-harmonic gyrotrons, J. Infrared Millim. Terahertz Waves **38**, 838 (2017).

[55] V. I. Shcherbinin, B. A. Kochetov, A. V. Hlushchenko, and V. I. Tkachenko, Cutoff frequencies of a dielectric-loaded rectangular waveguide with arbitrary anisotropic surface impedance, IEEE Trans. Microwave Theory Tech. **67**, 577 (2019).

[56] V. I. Shcherbinin, A. V. Hlushchenko, A. V. Maksimenko, and V. I. Tkachenko, Effect of cavity ohmic losses on

efficiency of low-power terahertz gyrotron, IEEE Trans. Electron Dev. **64**, 3898 (2017).

[57] C. Dragone, Reflection, transmission, and mode conversion in a corrugated feed, Bell Syst. Tech. J. **56**, 835 (1977).

[58] V. I. Shcherbinin, G. I. Zaginaylov, and V. I. Tkachenko, HE-and EH-hybrid waves in a circular dielectric waveguide with an anisotropic impedance surface, Prob. Atom. Sci. Tech. **98**, 89 (2015).

[59] Z. Sipus, M. Bosiljevac, and A. Grbic, Modelling cascaded cylindrical metasurfaces using sheet impedances and a transmission matrix formulation, IET Microw. Antennas Propag. **12**, 1041 (2018).

[60] V. I. Shcherbinin, G. I. Zaginaylov, and V. I. Tkachenko, Analogy between circular core-cladding and impedance waveguides and their membrane functions, Prog. Electromagn. Res. M **53**, 111 (2017).